ACS APPLIED MATERIALS & INTERFACES

www.acsami.org

Research Article

Route to High-Performance Micro-solid Oxide Fuel Cells on Metallic Substrates

Matthew P. Wells,* Adam J. Lovett, Thomas Chalklen, Federico Baiutti, Albert Tarancón, Xuejing Wang, Jie Ding, Haiyan Wang, Sohini Kar-Narayan, Matias Acosta, and Judith L. MacManus-Driscoll

Cite This: *ACS Appl. Mater. Interfaces* 2021, 13, 4117–4125

Read Online

ACCESS | Metrics & More | Article Recommendations | Supporting Information

ABSTRACT: Micro-solid oxide fuel cells based on thin films have strong potential for use in portable power devices. However, devices based on silicon substrates typically involve thin-film metallic electrodes which are unstable at high temperatures. Devices based on bulk metal substrates overcome these limitations, though performance is hindered by the challenge of growing state-of-the-art epitaxial materials on metals. Here, we demonstrate for the first time the growth of epitaxial cathode materials on metal substrates (stainless steel) commercially supplied with epitaxial electrolyte layers (1.5 μm $(Y_2O_3)_{0.15}(ZrO_2)_{0.85}$ (YSZ) + 50 nm CeO_2). We create epitaxial mesoporous cathodes of $(La_{0.60}Sr_{0.40})_{0.95}Co_{0.20}Fe_{0.80}O_3$ (LSCF) on the substrate by growing LSCF/MgO vertically aligned nanocomposite films by pulsed laser deposition, followed by selectively etching out the MgO. To enable valid comparison with the literature, the cathodes are also grown on single-crystal substrates, confirming state-of-the-art performance with an area specific resistance of 100 Ω cm^2 at 500 °C and activation energy down to 0.97 eV. The work marks an important step toward the commercialization of high-performance micro-solid oxide fuel cells for portable power applications.

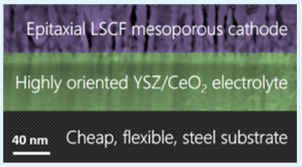

KEYWORDS: *solid oxide fuel cell, epitaxial thin film, metallic substrate, commercially viable, high-performance*

1. INTRODUCTION

Micro-solid oxide fuel cells (μSOFCs) are considered a promising future technology for portable power applications because of their efficiency and high energy density (up to 4 times higher than Li-ion batteries).[1] To achieve maximum efficiency, bulk SOFCs operate at temperatures in the region of 800 °C.[2] This, however, leads to both long start-up times and a lack of suitability to small-scale portable power applications, where devices require operation temperatures well below 500 °C.

Despite the many advances of μSOFCs,[1−3] two key challenges remain: (a) reducing the cell area specific resistances (ASRs), particularly the cathode ASR, so that cells can be operated below 500 °C and (b) improving device stability with temperature cycling. While μSOFCs on Si,[4,5] a commercially viable substrate with ease of device integration,[6,7] show good promise, there are problems of cyclability. Even when operating in the low-temperature regime of SOFCs (300−500 °C), Si-based devices are susceptible to strong degradation mainly due to the instability of thin-film metallic electrodes at intermediate-to-high temperature ranges.[2,8−10]

A possible strategy for achieving low ASRs at <500 °C, while maintaining good in-plane electrical conductivity for current collection and compatibility with thin-film technology, is the use of textured or epitaxial thin-film cathodes and electrolytes of low thickness.[11] Particularly, textured or epitaxial layers offer the advantage of a well-controlled geometry and microstructure, whether for the electrolyte, cathode, or both.[12−14] The highest power loss in a μSOFC is typically due to the oxygen reduction reaction (ORR) overpotential at the cathode, and there are therefore many reports of state-of-the-art epitaxial cathode thin films.[6,12,15,16] Primarily, μSOFCs have been fabricated on Si, but research has also focused on μSOFC fabrication on metal substrates to enable fast start-up times and superior mechanical stability and cyclability,[2,17,18] as discussed later.

As far as lowering the ASR of the electrolyte goes, control of grain boundaries and porosity in textured $(Y_2O_3)_{0.15}(ZrO_2)_{0.85}$ (YSZ) films has yielded values for activation energy and ionic conductivity of 1.04 eV and 0.02 S/m at 500 °C, respectively. These values are lower than those of the bulk material for which respective values of 1.18 eV and 0.1 S/m are reported.[19] Further, epitaxial YSZ films on Si have shown an activation energy of 0.79 eV and ionic conductivity of ∼0.003 S/m at 500 °C, marking further performance enhancements compared to textured films.[20] Exceptional improvements on electrolyte performance have also been achieved using vertically aligned nanocomposite (VAN) systems. More than an order of magnitude ionic conductivity was shown in several thin-film VAN systems (YSZ, $SrZO_3$, and Sm-doped CeO_2),[21−23] pointing toward the recent concept of room-temperature

Received: August 28, 2020
Accepted: December 24, 2020
Published: January 11, 2021

https://dx.doi.org/10.1021/acsami.0c15368
ACS Appl. Mater. Interfaces 2021, 13, 4117−4125

electrolytes.[24] However, to date, the superior performance of VAN films has only been demonstrated on single-crystal substrates.

As far as reducing the cathode ASR values and activation energies goes, epitaxial films of state-of-the-art cathode materials such as $(La_{0.60}Sr_{0.40})_{0.95}Co_{0.20}Fe_{0.80}O_3$ (LSCF) and $La_{0.7}Sr_{0.3}MnO_3$ are again typically grown on well lattice-matched single-crystal $SrTiO_3$, $NdGaO_3$, and $LaAlO_3$ substrates.[12,16] At 500 °C, the ASR values for LSCF are reported in the region of 10 Ω cm^2 with an activation energy between 1.2 and 1.7 eV.[25] Such epitaxial cathodes allow precise control of crystallographic planes at the surface, allowing substantial modification to reaction kinetics.[26,27] Meanwhile, VAN cathodes enable maximization of the reaction area and triple phase boundary.[28] Plonczak et al. demonstrate a reduction in the activation energy from 2.4 to 1.6 eV by introducing porosity to LSCF thin films, attributed to a reduction in the activation energy of the oxygen exchange process resulting from the increased catalytic surface area and to the activation of surface- or triple phase boundary (TPB)-related incorporation reactions.[29]

Fabricating μSOFCs on low-cost and flexible metal substrates such as Ni or stainless steel, with thermal expansion coefficients closely matching YSZ, overcomes the issues related to the use of unstable thin-film metals in Si, as well as the very different thermal expansions between the substrate and the electrolyte layer. Metal substrates also provide mechanical strength, high electrical conductivity, and good thermal conduction, enabling quick start-up times.[2,17,18] However, metal substrates tend to preclude the use of advanced, epitaxially grown, electrolyte and cathode materials. To our knowledge, no reports describe the growth of epitaxial electrolytes and cathodes on metal substrates. This is an essential challenge which must be overcome to enable the proliferation of high-performance, low-temperature μSOFCs, and this forms the focus of this study.

In the present work, we explore the use of metal substrates on which are grown highly biaxially oriented thin films of YSZ (1500 nm) and CeO_2 (50 nm) made using ion beam- or alternating beam-assisted deposition (ABAD), a scalable and cost-effective technique which has already found commercial applicability for the deposition of YSZ films in the superconductor industry.[30,31] We follow a μSOFC device fabrication procedure as set out in Figure 1. We show that mesoporous VAN LSCF cathodes of high quality can be easily grown on stainless steel substrates with biaxially textured YSZ electrolyte−CeO_2 bilayers prepared by ABAD. The mesoporous films of this study are fabricated by growth of LSCF/MgO VAN films and subsequent removal of the MgO by etching in acetic acid, resulting in epitaxial cathode films with a high catalytic surface area. After etching, we observe a reduction of ∼2 orders of magnitude in the ASR together with a reduced activation energy. These reductions are attributed to a combination of the increased surface area and modification to the oxygen ion incorporation path. It may be noted that, while strained CeO_2 shows good ionic conductivity, further performance enhancements can readily be achieved by doping.[32,33] We also demonstrate a simple means to chemically etch the stainless steel to allow gas access at the anode. Impedance measurements show that this μSOFC system is well-suited for low-temperature operation because of a low activation energy, resulting in a low cathode ASR in the 300−500 °C temperature range. The present work marks an important step toward the commercialization of high-performance μSOFCs for portable power applications.

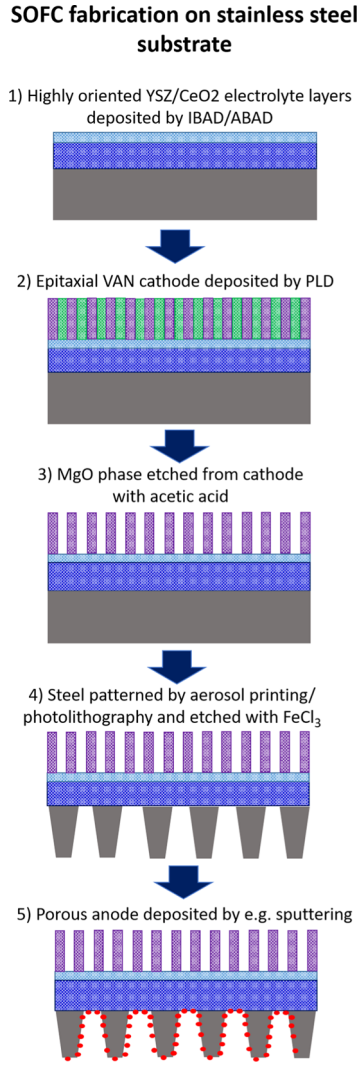

Figure 1. Schematic of the proposed fabrication procedure for μSOFCs incorporating VAN films on stainless steel substrates.

2. EXPERIMENTAL SECTION

Before determining the success of the μSOFC structure and properties, it was necessary to first assess the properties of the "ideal" VAN cathode of LSCF/MgO grown on single-crystal YSZ. We also grew films on single-crystal $(LaAlO_3)_{0.3}(Sr_2TaAlO_6)_{0.7}$ (LSAT) to determine whether a mesoporous honeycomb structure is not highly susceptible to lattice or structural mismatch effects and is hence a more universal approach which could later be applied to growth on a range of different electrolyte systems.

Cathode films were grown by pulsed laser deposition (PLD) on (100) oriented YSZ and (001) oriented LSAT substrates (and later on metal substrates as outlined below). The LSCF/MgO targets for the PLD growth were made by mixing 50:50 wt % $(La_{0.60}Sr_{0.40})_{0.95}Co_{0.20}Fe_{0.80}O_3$ (Fuel Cell Materials, Nexceris, LLC) and MgO powders (Alfa Aesar) in a rotary ball mill for ∼15 h. The mixed powders were pelletized into discs 12 mm in diameter and approximately 2 mm thick. The pellets were then placed in a 1500 bar cold isostatic press before sintering at 1300 °C for 4 h (heated and cooled at 5 °C/min).

Films were deposited at 750 °C in 0.4 mbar O_2 atmosphere with a flow rate of 9.8 sccm. The chamber was evacuated to at least 10^{-7} mbar before deposition. A composite ceramic target, held 45 mm

https://dx.doi.org/10.1021/acsami.0c15368
ACS Appl. Mater. Interfaces 2021, 13, 4117−4125

from the substrates, was ablated with a 248 nm laser (Lambda Physik, Inc.) with a repetition rate of 3 Hz and a fluence of approximately 0.8 J/cm^2. Samples were cooled to room temperature in the same 0.4 mbar O_2 atmosphere at 10 °C/min.

The procedure for the fabrication of the μSOFCs (shown schematically in Figure 1) is as follows:

Step 1—metal/electrolyte substrates: Commercial (Bruker) stainless steel substrates (0.1 mm) were sourced with biaxially textured YSZ (1500 nm) and CeO_2 (50 nm) layers prepared by ABAD.

Step 2—deposition of VAN cathodes: VAN cathode films were deposited on the ABAD-buffered stainless steel substrates by PLD using the same parameters described above for the single-crystal substrates.

Step 3—etching the VAN cathodes: MgO was etched out of the VAN film using 3.3 M solution of acetic acid, stirred at 60 rpm for 17 min, to leave a mesoporous LSCF cathode.

Step 4—etching holes in the stainless steel: The stainless steel was patterned to give a mask of ~100 μm diameter holes spaced ~500 μm apart. Experiments were conducted into the use of both photolithography and aerosol printing. For the latter, the mask was created using an Optomec AJ200 aerosol jet printer with a design created in AutoCAD 2018. An ink of poly(vinylidene difluoride) (PVDF)-TrFE was prepared by dissolving PVDF-TrFE (70/30 wt %, Piezotech) in *N*-methyl-2-pyrrolidone (Sigma-Aldrich) at 5 wt % under constant stirring at 60 °C. The stainless steel substrate was immobilized on the printer platen, with the platen temperature set at 40 °C. Approximately, 20 mL of PVDF-TrFE ink was loaded into the bottle for the pneumatic atomizer. Using a 250 μm nozzle, the ink was printed with an atomizing flow rate of 1500 sccm, an exhaust flow rate of 1450 sscm, and a sheath flow rate of 150 sscm. The design was followed 40 times in order to build up sufficient thickness to ensure mechanical stability. The substrate was then dried in an oven at 130 °C for 2 h. Further details of this process are described in previous work.[34] 0.3 M $FeCl_3$ solution was used to etch regions where the resist/mask was not present (step 3). $FeCl_3$ is known to selectively etch the stainless steel while leaving YSZ unaffected, as demonstrated by Chen et al.[35] Holes are needed (as closely spaced as possible without degrading the structural integrity of the substrate) to enable gas (e.g., H_2) access at the anode to the electrolyte. Solution etching rates are typically much higher than those of physical etching techniques such as reactive ion etching and ion milling (the latter giving an etch rate of approximately 1 μm/h for stainless steel[36]), making it the practical option for etching a 100 μm thick substrate. The disadvantage in this case is the isotropic nature of the etch. This can be mitigated by adopting a three-step procedure as demonstrated by Shimizu et al., though to date, this has only been applied to much thinner substrates ~500 nm.[37] Samples were etched for approximately 5 h at 70 °C and stirred at 60 rpm for the first 4 h.

X-ray diffraction (XRD) measurements for samples on single-crystal substrates were conducted using a Panalytical Empyrean high-resolution X-ray diffractometer using Cu Kα radiation (λ = 1.5405 Å). Samples on the ABAD-buffered stainless steel were characterized using a Bruker D8 diffractometer (Cu Kα radiation, λ = 1.5405 Å).

Atomic force microscopy (AFM) measurements were performed on films using a Bruker Multimode 8 system in the tapping mode. Commercial silicon cantilevers (Budget Sensors Ltd.) with a resonance frequency of 300 kHz and a spring constant of 40 N/m were used to image 0.5 μm^2 areas at a scan frequency of 1 Hz. A conducting cobalt−chromium-coated silicon cantilever with a resonance frequency of 150 kHz and a spring constant of 5 N/m was used for Kelvin probe force microscopy (KPFM) measurements.

Impedance measurements on the electrolyte structure were carried out using a probe station and a hot plate together with a HP4294A impedance analyzer. Regiments were conducted over a frequency range of 40 Hz to 1 MHz with a 50 mV AC voltage. The stainless steel substrate was grounded, and a voltage was applied to a circular Pt top electrode deposited by DC magnetron sputtering with a radius of approximately 250 μm defined by the shadow mask.

Impedance spectroscopy measurements on the LSCF mesoporous cathode (deposited on single crystal YSZ) were carried out in a test station using Ag as a porous low impedance counter electrode and a synthetic air atmosphere. Porous Au paste was applied on the electrode surface as a current collector. Measurements were conducted in the out-of-plane direction, and impedance spectra were acquired using an Alpha-A Novocontrol impedance spectrometer with the ZG4 test interface in the frequency range of 10^6 to 0.1 Hz and with a voltage amplitude of 0.05 V. For the fitting of the impedance data related to the cathode polarization arc, an equivalent circuit composed of a series of two ZARC elements (resistance in parallel to a constant phase element) was used, being the simplest circuit able to fit the experimental data. The ASR was calculated considering the area of the Au current collector (projected area of the cathode).

3. RESULTS AND DISCUSSION

The LSCF/MgO cathode was first characterized by XRD following the deposition on single-crystal (100) 8-YSZ substrates and ABAD-buffered stainless steel substrates. In both cases, the films are highly oriented and epitaxial. Figure S1 shows the XRD patterns of the LSCF/MgO film on (100) 8-YSZ. The film is oriented along the (110) axis as expected for the growth of a perovskite material (a_{LSCF} = 3.8−3.9 Å) on 8-YSZ (a_{YSZ} = 5.14 Å).[38] Here, 3.93 × $\sqrt{2}$ = 5.54 giving a lattice mismatch of 7.2%, indicating domain matching epitaxy.[13,39] A 45° rotation relative to the substrate is confirmed by in-plane XRD (phi scan) shown in Figure S2. Figures S3 and S4, respectively, show comparative XRD for the cathode grown on the ABAD-buffered stainless steel substrate (after step 2 in Figure 1) and on $Ce_{0.8}Gd_{0.2}O_2$-buffered single-crystal YSZ (as used for subsequent impedance measurements). In both cases, the same predominant (110) orientation of the LSCF is confirmed, with additional contributions from the (111) orientation. Here, we note the poor visibility of the (220) LSCF peak (theoretical position ~ 69.2°) due to overlap with CeO_2 (400) at 69.29°. In LSCF, the (110) orientation is desirable as computational studies predict a higher catalytic activity for oxygen reduction from the (110) surface of perovskite oxides,[40,41] while experimental data demonstrate the surface exchange coefficient k^* to be approximately 1 order of magnitude higher for (110)-oriented LSCF thin films (k^* ~ 7.3 × 10^{-6} cm s^{-1}) than for (100)-oriented samples (k^* ~ 0.7 × 10^{-6} cm s^{-1}).[42] It is important to note that it is difficult to achieve a single orientation of thin-film materials which are astructural to the substrate. This is the case for both LSCF (perovskite) and MgO (rock salt) on the YSZ (fluorite) substrate and for MgO on the LSAT (perovskite) substrate. This is discussed further in our previous works.[43,44] XRD measurements of the etched films (after step 3) (Figures S1 and S3−S5) confirm that the MgO is removed by the etching process, leaving the LSCF structurally intact as discussed elsewhere.[45] Further, films were grown on single-crystal (001) LSAT substrates (Figure S5) which, with a lattice parameter of 3.87 Å, match exactly 3.87 Å for bulk LSCF. Also, LSAT is structural to LSCF (both are perovskite) and thus enables growth of very highly aligned and highly crystalline VAN films.

Scanning electron microscopy (SEM), AFM, and transmission electron microscopy (TEM) images showing film cross-sections before and after etching are shown in Figure 2. Figure 2a,b shows the top-down SEM images before and after etching, where we observe dense and mesoporous films, respectively, from representative films grown on single-crystal YSZ substrates. Sample porosity was evaluated using SEM

https://dx.doi.org/10.1021/acsami.0c15368
ACS Appl. Mater. Interfaces 2021, 13, 4117−4125

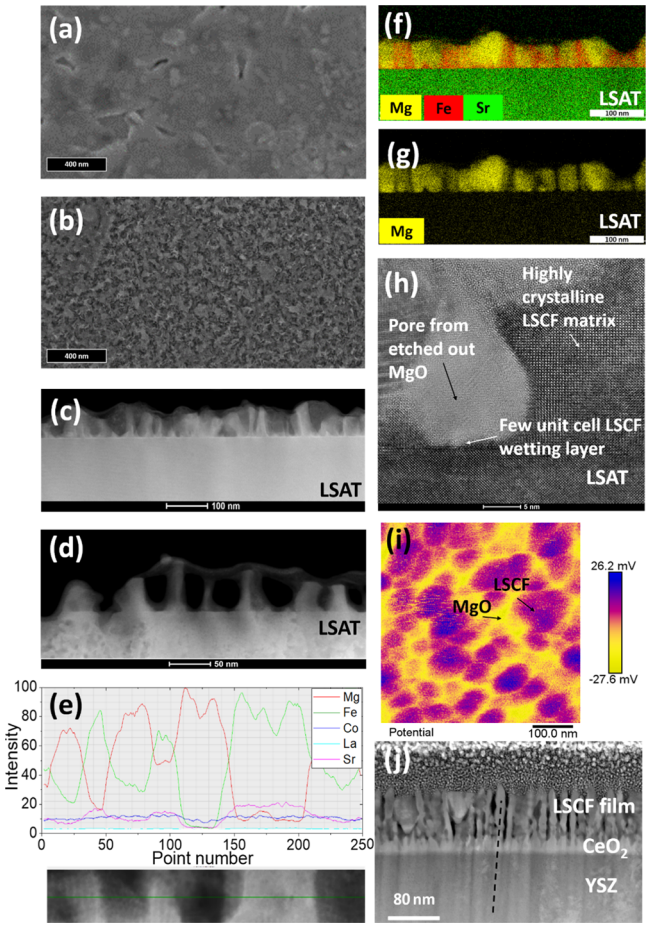

Figure 2. (a,b) Top-down SEM images of films grown on single-crystal YSZ before and after etching. (c,d) HAADF images of films grown on LSAT before and after etching. (e) EDX scan profile film before etching. (f,g) EDX measurements of the LSCF/MgO film before etching of MgO. (h) TEM image of the film after etching of MgO. (i) KPFM image of the LSCF/MgO cathode grown on ABAD-buffered stainless steel. (j) TEM image of the film grown on ABAD-buffered stainless steel after etching of MgO.

image analysis software (MountainsLab, version 8.2), as shown in Figure S6, from which the porosity is calculated as 47%. As with the growth on ABAD-buffered stainless steel (Figures S7 and S8), we observe a mesoporous matrix. The lateral feature dimensions are similar to those measured on LSAT substrates, in the range of ∼30 nm (minimum distance observed ∼ 15 nm; maximum distance ∼ 40 nm). Figure 2c,d shows the representative high-angle annular dark field (HAADF) images of films grown on LSAT before and after etching, respectively. Figure 2e shows the composition of the columns from EDX analysis. The results demonstrate that the etching process is selective to the MgO and that epitaxy of the LSCF is maintained, allowing a greater surface area for the ORR to occur.

Figure 2f,g shows the EDX maps before etching of a film on an LSAT substrate. The MgO regions are very clearly differentiated from the matrix. The high-resolution TEM image of an etched film on an LSAT substrate (Figure 2h) shows that after etching out the MgO, a highly ordered perovskite LSCF matrix remains, and hence it is not perturbed by the etching. Also, where the MgO is removed, a perfect bulb-shaped pore remains. The reason for this feature can be understood by explaining the growth process of VAN films for approximately equal volume percentages of phases: laser ablation of a mixed phase target leads to self-assembled growth of a film comprised of a matrix phase and nanopillars embedded within the matrix phase, formed by nucleation and growth.[46−48]

Since the LSCF has the same perovskite crystal structure as the LSAT substrate and also has similar lattice parameters (3.87 Å), it has a low interfacial energy with the LSAT substrate. Hence, after adatom diffusion of the ablated species on the substrate surface, LSCF forms the initial layer on the substrate since it can wet it easily. On the other hand, the dissimilar crystal structure of the MgO (rock salt) and its larger lattice parameter of 4.2 Å[49] means that it wets the substrate poorly. However, after the initial growth of a few unit cells of the LSCF film (as labelled in Figure 2h), the MgO concentration in the layer above this initial layer will be higher than the bulk ratio. This will lead to a strong driving force for MgO nucleation on the initial LSCF surface layers. Once nucleated, the individual phases will lead to growth of the same species on their surfaces since these will have the lowest interfacial energies. Hence, MgO will grow on the preformed MgO and LSCF will grow on the preformed LSCF. The phases will grow in the direction of the incoming species, that is, perpendicular to the substrate, in the form of columns. Since the LSCF nucleated on the substrate, the columns will be joined and thus produce a connected matrix. On the other hand, the MgO columns are not connected and so form isolated pillar structures. The MgO pillars have a bulbous appearance owing to them not wetting the substrate. Since the pillars punctuate the matrix, the matrix is in a honeycomb form rather than a simple planar form.

Figure S9 shows further the EDX analysis of the film of Figure 2f, confirming all chemical elements present in the LSCF matrix, without Mg substitution, and only the Mg cation present in the MgO nanopillars.

Figure 2(i) shows the KPFM image of a VAN film on ABAD-buffered stainless steel before removal of the MgO by etching. This confirms two distinct material phases in an approximately honeycomb structure of the matrix material. Further AFM images shown in Figure S7 show samples grown on single-crystal YSZ [with a $Ce_{0.8}$ $Gd_{0.2}O_2$ (thickness ≈ 10 nm) buffer layer] before (Figure S7a) and after (Figure S7b) etching, while Figure S7c,d shows the equivalent images for films on ABAD-buffered stainless steel. These images confirm the removal of one material phase to leave a porous structure, as observed in previous works,[50] with features of similar size (after step 3), independent of the form of the YSZ substrate, whether ABAD or single crystal. The equivalent 3D representations of these figures are given in the Supporting Information (Figure S8).

Finally, Figure 2j shows the TEM image of the etched film grown on ABAD-buffered stainless steel. As shown by the dashed line passing through the film layers, we observe that the LSCF columnar regions nucleate on the CeO_2 columns (which themselves nucleate on the YSZ). Hence, it appears that the LSCF, rather than MgO, nucleates preferentially on the fluorite-structured CeO_2 to form the matrix phase. Nucleation of perovskites on fluorite substrates has been demonstrated previously using PLD, with lattice matching facilitated by a 45° in-plane rotation of the (100) aligned crystals to closely match the (100) fluorite surface.[13] We note that the feature size observed by TEM after etching is significantly smaller than that

https://dx.doi.org/10.1021/acsami.0c15368
ACS Appl. Mater. Interfaces 2021, 13, 4117−4125

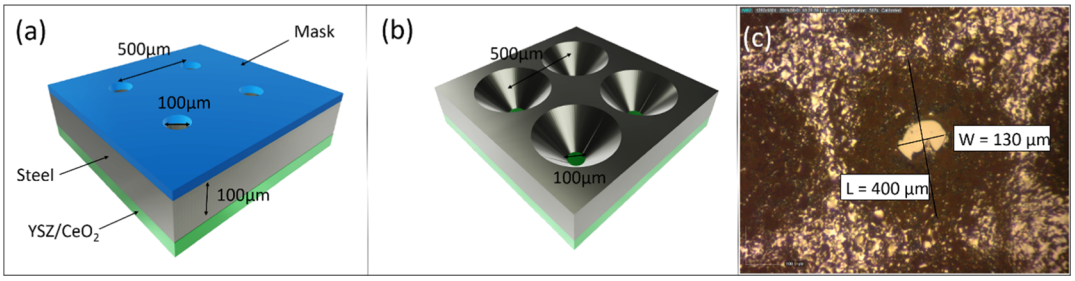

Figure 3. Schematics of the etching process of step 4 showing the (a) sample with mask applied before etching and (b) sample after etching. (c) 100 μm holes etched using aerosol-printed polymer mask—electrolyte layer collapsed.

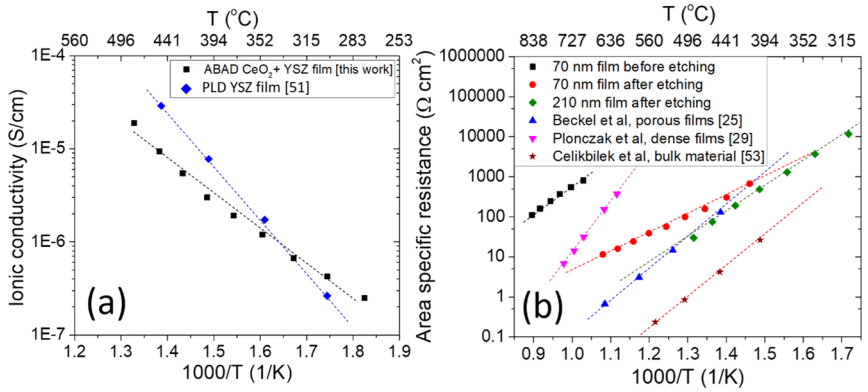

Figure 4. Electrical data of electrolyte and cathode layers. (a) Arrhenius plot of ionic conductivity of YSZ films deposited by ABAD on stainless steel;[51] (b) ASR of the LSCF/MgO film before and after etching of MgO as compared to the literature results from Beckel et al.,[25] Plonczak et al.,[29] and Çelikbilek et al.[53]

observed by KPFM (~30 nm) before etching. This is understood because KPFM does not measure microstructural boundaries and has a lower spatial resolution (~30 nm, cf ~ 0.1 nm for TEM). The selective removal of MgO upon etching is again confirmed by EDX analysis (Figure S10).

We now explore the etching of the metallic substrate (after step 4 in Figure 1). Figure 3a shows a schematic of the mask pattern, with ~100 μm holes spaced ~500 μm apart, to be implemented by aerosol printing. Figure 3b schematically shows complete etching with $FeCl_3$ giving cones of steel etched to the YSZ and with the 8-YSZ intact at the base of the cones. Figure 3c shows an actual image viewed from the metal surface after 5 h of etching. Etching was performed after deposition of the cathode layer, with the sample mounted in a custom-made support to ensure $FeCl_3$ access to only the stainless steel, protecting the cathode layer. Provisional experiments confirmed that the $FeCl_3$ terminated at the 8-YSZ interface and that the electrolyte layer was able to self-support over a 300 × 100 μm^2 area. While fragile free-standing YSZ regions after the etching did not retain perfection over the whole film area (Figure 3c), the proof-of-concept of the simple etching process was demonstrated. Further improvements in the process are highly possible using several-step etching procedures.[37] Moreover, the film growth techniques demonstrated in this work could readily be implemented on novel substrates, for instance, nanoporous Ni, on which virtually pore-free electrolytes can be deposited by PLD, thus allowing gas access without the need for etching and further enhancing the commercial applicability of this work.[2,37]

Having demonstrated the growth of mesoporous VAN cathodes on both single-crystal and metal substrates and the ability to etch holes in the stainless steel substrate, we now turn to the electrical performance of the films. Figure 4a shows the results of ionic conductivity measurements as a function of temperature for the CeO_2/YSZ films on stainless steel determined from electrochemical impedance spectroscopy (EIS) (Figure S11). The data were acquired between 275 and 480 °C to approximate the low-temperature operating regime of a μSOFC. The ionic conductivity and E_a (0.79 eV) are comparable to literature values, thus showing the high quality of the films and confirming the validity of this approach for the fabrication of μSOFCs.[51] It may be noted that E_a is markedly lower than the values typically reported for bulk YSZ (>1 eV); multiple reports however describe activation energies for thin-film YSZ samples in the 0.6−1 eV region. The reduction in the activation energy has been ascribed to multiple factors including strain, film defects, and influence of interfacial versus bulk conduction mechanisms.[51]

The ASR of the thin-film cathodes was measured by growing the thin film on one side of a YSZ substrate [with a $Ce_{0.8}Gd_{0.2}O_2$ (thickness ≈ 10 nm) buffer layer to reduce substrate—film lattice mismatch and to avoid the formation of secondary phases at the interface] and depositing a low impedance, porous Ag counter electrode on the other (see Figure S12 for representative Nyquist plots and impedance fittings). In this way, the impedance response is dominated by the thin-film cathode.[52] Figure 4b shows the ASR of a 70 nm film measured as a function of temperature before and after the MgO was removed by etching in acetic acid. To give relevant comparisons, the results of this work are compared to literature values for LSCF thin films, both dense (Plonczak et al.[29]) and porous (Beckel et al.[25]), as well as for porous bulk samples (Çelikbilek et al.[53]). For bulk LSCF samples, the E_a values typically reported range from ~0.44[54] to ~1.5 eV[53] compared

https://dx.doi.org/10.1021/acsami.0c15368
ACS Appl. Mater. Interfaces 2021, 13, 4117−4125

to ~2.4 eV for dense thin films and ~1.6 eV for porous thin films.[29] The differences between these different material forms have previously been attributed to the different levels of stress/strain and defects, although more work is needed to fully understand these separate effects. For our VAN nanoporous films, the comparative influences of porosity and etching will be presented in more detail in a separate study.

Before etching, the presence of the MgO (which is inert toward ORR[55]) results in ASR values of approximately 100 Ω cm^2 at 840 °C, several orders of magnitude higher than that observed for plain LSCF films in the literature (as shown by the pink and blue lines in Figure 4b). Additionally, Figure 4b shows the ASR values of etched films with thicknesses of 70 and 210 nm.

In-plane tensile strain is known to induce Sr surface segregation,[38,56] resulting in electronically and ionically insulating Sr-enriched phases, which severely impede surface oxygen exchange.[57] However, in the temperature range studied here, this is expected to be a small effect; for example, Jung and Tuller observed no significant change in either surface Sr content or impedance below 560 °C in thin-film $SrTi_{1-x}Fe_xO_3$ samples, which are studied as a model system for mixed ionic electronic conducting perovskite cathodes.[58] Moreover, from the reciprocal space maps presented in Figure S13, we calculate the in-plane lattice parameters as $a = b = 3.897 \pm 0.004$ Å before etching and 3.904 ± 0.004 Å after etching. There is no clear change (within error) in the in-plane tensile strain.

For completeness, the out-of-plane strain change was also determined before and after etching. This was done by using θ–2θ XRD scans. An out-of-plane tension was observed in the as-grown VAN film, as expected because of the presence of stiff and larger lattice parameter MgO *cf.* LSCF (i.e., 4.21 Å compared to ~3.8–3.9 Å[38,49]). For a VAN film on a YSZ single-crystal substrate, Figure S1 shows a shift in the X-ray peak position of the LSCF (110) peak to give $(a + b)/2 = 3.922 \pm 0.002$ Å before etching to 3.913 ± 0.002 Å after etching. This indicates that the tensile strain state was at least partially relaxed after etching out the MgO, as shown in the schematic of Figure 5. The same level of strain relaxation was also observed on the ABAD-buffered stainless steel. We note that since the lattice parameters of LSCF are dependent upon its precise composition varying by around 0.1 Å for different cation stoichiometries, it is not possible to ascertain the level of strain compared to bulk LSCF.[38]

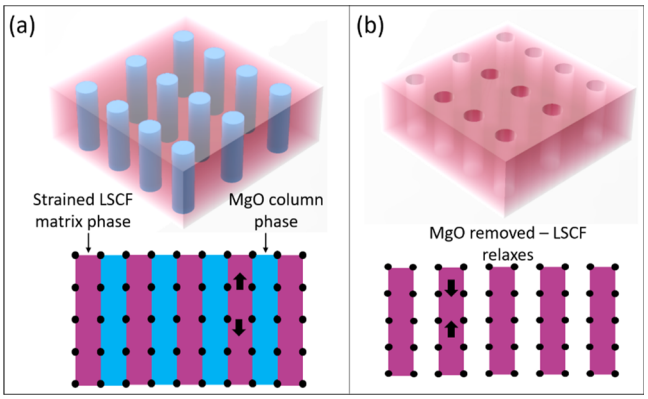

Figure 5. (a) LSCF/MgO VAN film and (b) strain relaxation after etching MgO.

After etching the 70 nm film, a substantial decrease is observed in both the value of ASR [from approximately 70,000 Ω cm^2 (linearly extrapolated value) at 500 °C before etching to 100 Ω cm^2 after etching] and the activation energy (E_a) from 1.6 ± 0.1 eV before etching to 0.97 ± 0.01 eV after etching, leading, at <~400 °C, to lower values of ASR than for plain LSCF films.

While a decrease in the ASR upon etching the 70 nm film could be in principle explained by a higher surface area available for the solid–gas reaction, the lower E_a value suggests a more subtle change in the oxygen incorporation kinetics upon etching. Particularly, the highly distorted impedance spectrum of the etched material (Figure S14) suggests the presence of an electrode process which, upon chemical treatment, becomes colimited by diffusion and solid–gas reactions.[59] Assuming that, in the case of etched material, oxygen incorporation is colimited as described above, the different activation energy for the 70 nm etched film with respect to the 500 nm etched film may be related to microstructural aspects (e.g., porosity gradients along the electrodes thickness or microstructural differences between the samples), which determine the occurrence of oxide ion transport via bulk or surface paths.[60] A change in the surface stoichiometry of the LSCF by the etching process is also a possibility. In fact, as observed from Figure 2h, the LSCF matrix is highly intact with no reaction products visible on the LSCF surface after etching. The atomic scale information about the chemical etching effect is beyond the scope of this study and is dealt with in other separate studies.[45]

Comparing the ASR values for etched 70 and 210 nm films, at 450 °C, the 70 nm film offers ~275 Ω cm^2, while the 210 nm film gives ~85 Ω cm^2; with an E_a ~ 1.5 eV, this linearly extrapolates to ~1 Ω cm^2 at 600 °C, in line with the state-of-the-art performance of porous LSCF.[25] For temperatures <400 °C, however, the lower activation energy of the 70 nm film once again yields a lower ASR. Since, to the best of our knowledge, the results of Beckel et al.[25] mark the lowest reported for LSCF thin films, this result is important for μSOFCs for operation below 400 °C. Further, by demonstrating the growth of the VAN cathode films on commercially sourced metal substrates, complete with the electrolyte layer, the present work identifies a commercially viable route to the fabrication of high-performance μSOFCs for low-temperature portable applications. The different activation energy for the 70 nm etched film with respect to the 210 nm etched film again suggests the presence of two different oxide ion transport paths (bulk and surface), the latter becoming predominant for low electrode thicknesses.[60] A further detailed electrochemical study will be conducted next to further elucidate the effect of film thickness on the dominant transport path.

4. CONCLUSIONS

We have shown that it is possible to grow state-of-the-art epitaxial, mesoporous LSCF thin film cathodes on commercially available stainless steel metallic substrates with biaxially aligned YSZ electrolyte layers. First, we demonstrated that the commercially available YSZ electrolytes on stainless steel feature 3×10^{-6} S·cm^{-1} ionic conductivity at 400 °C. Such a performance is consistent with typical high-performance materials used for electrochemical devices. Thereafter, we showed that epitaxial, porous LSCF cathodes feature an ASR of 100 Ω cm at 500 °C and an activation energy of 0.97 eV, demonstrating state-of-the-art performance. Finally, we showed

https://dx.doi.org/10.1021/acsami.0c15368
ACS Appl. Mater. Interfaces 2021, 13, 4117–4125

that it is possible to pattern and chemically etch holes of ~100 μm dimension into the μSOFC device for allowing gas access. Our work marks an important advance toward creating high-performance μSOFCs for portable power applications via a proven commercial metallic substrate system.

■ ASSOCIATED CONTENT

Supporting Information

The Supporting Information is available free of charge at https://pubs.acs.org/doi/10.1021/acsami.0c15368.

XRD measurements, in-plane scans, AFM images, porosity analysis, HAADF and EDX images, EDX measurements, representative Nyquist plots, reciprocal space maps, and distorted impedance spectrum (PDF)

■ AUTHOR INFORMATION

Corresponding Author

Matthew P. Wells − *Department of Materials Science and Metallurgy, University of Cambridge, Cambridge CB3 0FS, U.K.*; orcid.org/0000-0003-2632-0160; Email: mpw52@cam.ac.uk

Authors

Adam J. Lovett − *Department of Materials Science and Metallurgy, University of Cambridge, Cambridge CB3 0FS, U.K.*

Thomas Chalklen − *Department of Materials Science and Metallurgy, University of Cambridge, Cambridge CB3 0FS, U.K.*

Federico Baiutti − *Department of Advanced Materials for Energy, Catalonia Institute for Energy Research (IREC), Barcelona 08930, Spain*; orcid.org/0000-0001-9664-2486

Albert Tarancón − *Department of Advanced Materials for Energy, Catalonia Institute for Energy Research (IREC), Barcelona 08930, Spain; ICREA, Barcelona 08010, Spain*; orcid.org/0000-0002-1933-2406

Xuejing Wang − *School of Materials Engineering, Purdue University, West Lafayette, Indiana 47907-2045, United States*

Jie Ding − *School of Materials Engineering, Purdue University, West Lafayette, Indiana 47907-2045, United States*

Haiyan Wang − *School of Materials Engineering, Purdue University, West Lafayette, Indiana 47907-2045, United States*; orcid.org/0000-0002-7397-1209

Sohini Kar-Narayan − *Department of Materials Science and Metallurgy, University of Cambridge, Cambridge CB3 0FS, U.K.*; orcid.org/0000-0002-8151-1616

Matias Acosta − *Department of Materials Science and Metallurgy, University of Cambridge, Cambridge CB3 0FS, U.K.*

Judith L. MacManus-Driscoll − *Department of Materials Science and Metallurgy, University of Cambridge, Cambridge CB3 0FS, U.K.*

Complete contact information is available at: https://pubs.acs.org/10.1021/acsami.0c15368

Author Contributions

The manuscript was written through contributions of all authors. All authors have given approval to the final version of the manuscript. Samples were grown by M.P.W. and M.A.; XRD and AFM measurements were conducted by M.P.W., A.J.L., and M.A.; EIS measurements were done by M.P.W. and A.J.L.; ASR measurements were done by F.B.; TEM and EDX were performed by H.W., J.D., and X.W.; aerosol printing was conducted by T.C.

Funding

We acknowledge substrate provision from Bruker HTS via our H2020 project Eurotapes, EUROTAPES, a collaborative project funded by the European Commission's Seventh Framework Program (FP7/2007−2013) under grant agreement no. 280432. J.L.M.-D. and M.P.W. acknowledge the ERC POC grant, Portapower, 779444. J.L.M.-D. also acknowledges support from the Royal Academy of Engineering Chair in Emerging technologies grant CIET1819_24 and the EPSRC Centre of Advanced Materials for Integrated Energy Systems (CAM-IES), grant EP/P007767/1. M.A. acknowledges support from the Feodor Lynen Research Fellowship Program of the Alexander von Humboldt Foundation and the Isaac Newton Trust 17.25(a) and support from the Centre of Advanced Materials for Integrated Energy Systems (CAM-IES) under EP/P007767/1. S.K.-N. acknowledges support from the European Research Council through an ERC Starting Grant (ERC-2014-STG-639526, NANOGEN). The TEM/HRTEM work at Purdue University was supported by the U.S. National Science Foundation (DMR-1565822 and DMR-2016453). Part of this project has received funding from the European Union's Horizon 2020 research and innovation program under grant agreement no 824072 (HARVESTORE) and no 681146 (ULTRASOFC) and was supported by an STSM grant from the COST Action MP1308: towards oxide-based electronics (TO-BE) supported by COST (European Cooperation in Science and Technology).

Notes

The authors declare no competing financial interest.

■ REFERENCES

(1) Bieberle-Hütter, A.; Beckel, D.; Infortuna, A.; Muecke, U. P.; Rupp, J. L. M.; Gauckler, L. J.; Rey-Mermet, S.; Muralt, P.; Bieri, N. R.; Hotz, N.; Stutz, M. J.; Poulikakos, D.; Heeb, P.; Müller, P.; Bernard, A.; Gmür, R.; Hocker, T. A Micro-Solid Oxide Fuel Cell System as Battery Replacement. *J. Power Sources* **2008**, *177*, 123−130.

(2) Lee, Y.; Park, Y. M.; Choi, G. M. Micro-Solid Oxide Fuel Cell Supported on a Porous Metallic Ni/stainless-Steel Bi-Layer. *J. Power Sources* **2014**, *249*, 79−83.

(3) Kwon, C.-W.; Son, J.-W.; Lee, J.-H.; Kim, H.-M.; Lee, H.-W.; Kim, K.-B. High-Performance Micro-Solid Oxide Fuel Cells Fabricated on Nanoporous Anodic Aluminum Oxide Templates. *Adv. Funct. Mater.* **2011**, *21*, 1154−1159.

(4) Pihlatie, M.; Ramos, T.; Kaiser, A. Testing and Improving the Redox Stability of Ni-Based Solid Oxide Fuel Cells. *J. Power Sources* **2009**, *193*, 322−330.

(5) Al-Khori, K.; Bicer, Y.; Koç, M. Integration of Solid Oxide Fuel Cells into Oil and Gas Operations: Needs, Opportunities, and Challenges. *J. Cleaner Prod.* **2020**, *245*, 118924.

(6) Garbayo, I.; Pla, D.; Morata, A.; Fonseca, L.; Sabaté, N.; Tarancón, A. Full Ceramic Micro Solid Oxide Fuel Cells: Towards More Reliable MEMS Power Generators Operating at High Temperatures. *Energy Environ. Sci.* **2014**, *7*, 3617−3629.

(7) Huang, H.; Nakamura, M.; Su, P.; Fasching, R.; Saito, Y.; Prinz, F. B. High-Performance Ultrathin Solid Oxide Fuel Cells for Low-Temperature Operation. *J. Electrochem. Soc.* **2007**, *154*, B20.

(8) Watanabe, H.; Yamada, N.; Okaji, M. Linear Thermal Expansion Coefficient of Silicon from 293 to 1000 K. *Int. J. Thermophys.* **2004**, *25*, 221−236.

(9) Yamamoto, O. Solid Oxide Fuel Cells: Fundamental Aspects and Prospects. *Electrochim. Acta* **2000**, *45*, 2423−2435.

(10) Baertsch, C. D.; Jensen, K. F.; Hertz, J. L.; Tuller, H. L.; Vengallatore, S. T.; Spearing, S. M.; Schmidt, M. A. Fabrication and Structural Characterization of Self-Supporting Electrolyte Membranes for a Micro Solid-Oxide Fuel Cell. *J. Mater. Res.* **2004**, *19*, 2604−2615.
(11) Acosta, M.; Baiutti, F.; Tarancón, A.; MacManus-Driscoll, J. L. Nanostructured Materials and Interfaces for Advanced Ionic Electronic Conducting Oxides. *Adv. Mater. Interfaces* **2019**, *6*, 1900462.
(12) Santiso, J.; Burriel, M. Deposition and Characterisation of Epitaxial Oxide Thin Films for SOFCs. *J. Solid State Electrochem.* **2011**, *15*, 985−1006.
(13) Mori, D.; Oka, H.; Suzuki, Y.; Sonoyama, N.; Yamada, A.; Kanno, R.; Sumiya, Y.; Imanishi, N.; Takeda, Y. Synthesis, Structure, and Electrochemical Properties of Epitaxial Perovskite La0.8Sr0.2-CoO3 Film on YSZ Substrate. *Solid State Ionics* **2006**, *177*, 535−540.
(14) Sanna, S.; Esposito, V.; Pergolesi, D.; Orsini, A.; Tebano, A.; Licoccia, S.; Balestrino, G.; Traversa, E. Fabrication and Electrochemical Properties of Epitaxial Samarium-Doped Ceria Films on SrTiO3-Buffered MgO Substrates. *Adv. Funct. Mater.* **2009**, *19*, 1713−1719.
(15) Shao, Z.; Haile, S. M. A High-Performance Cathode for the next Generation of Solid-Oxide Fuel Cells. *Nature* **2004**, *431*, 170−173.
(16) Zomorrodian, A.; Salamati, H.; Lu, Z.; Chen, X.; Wu, N.; Ignatiev, A. Electrical Conductivity of Epitaxial La0.6Sr 0.4Co0.2Fe0.8O3-δ Thin Films Grown by Pulsed Laser Deposition. *Int. J. Hydrogen Energy* **2010**, *35*, 12443−12448.
(17) Joo, J. H.; Choi, G. M. Simple Fabrication of Micro-Solid Oxide Fuel Cell Supported on Metal Substrate. *J. Power Sources* **2008**, *182*, 589−593.
(18) Vafaeenezhad, S.; Sandhu, N. K.; Hanifi, A. R.; Etsell, T. H.; Sarkar, P. Development of Proton Conducting Fuel Cells Using Nickel Metal Support. *J. Power Sources* **2019**, *435*, 226763.
(19) Rey-Mermet, S.; Yan, Y.; Sandu, C.; Deng, G.; Muralt, P. Nanoporous YSZ Film in Electrolyte Membrane of Micro-Solid Oxide Fuel Cell. *Thin Solid Films* **2010**, *518*, 4743−4746.
(20) Jiang, J.; Hu, X.; Shen, W.; Ni, C.; Hertz, J. L. Improved Ionic Conductivity in Strained Yttria-Stabilized Zirconia Thin Films. *Appl. Phys. Lett.* **2013**, *102*, 143901.
(21) Yang, S. M.; Lee, S.; Jian, J.; Zhang, W.; Lu, P.; Jia, Q.; Wang, H.; Won Noh, T.; Kalinin, S. V.; MacManus-Driscoll, J. L. Strongly Enhanced Oxygen Ion Transport through Samarium-Doped CeO2 Nanopillars in Nanocomposite Films. *Nat. Commun.* **2015**, *6*, 8588.
(22) Lee, S.; MacManus-Driscoll, J. L. Research Update: Fast and Tunable Nanoionics in Vertically Aligned Nanostructured Films. *APL Mater.* **2017**, *5*, 042304.
(23) Lee, S.; Zhang, W.; Khatkhatay, F.; Wang, H.; Jia, Q.; Macmanus-Driscoll, J. L. Ionic Conductivity Increased by Two Orders of Magnitude in Micrometer-Thick Vertical Yttria-Stabilized ZrO2 Nanocomposite Films. *Nano Lett.* **2015**, *15*, 7362−7369.
(24) Garbayo, I.; Chiabrera, F.; Alayo, N.; Santiso, J.; Morata, A.; Tarancón, A. Thin Film Oxide-Ion Conducting Electrolyte for near Room Temperature Applications. *J. Mater. Chem. A* **2019**, *7*, 25772−25778.
(25) Beckel, D.; Muecke, U.; Gyger, T.; Florey, G.; Infortuna, A.; Gauckler, L. Electrochemical Performance of LSCF Based Thin Film Cathodes Prepared by Spray Pyrolysis. *Solid State Ionics* **2007**, *178*, 407−415.
(26) Tsvetkov, N.; Lu, Q.; Sun, L.; Crumlin, E. J.; Yildiz, B. Improved Chemical and Electrochemical Stability of Perovskite Oxides with Less Reducible Cations at the Surface. *Nat. Mater.* **2016**, *15*, 1010−1016.
(27) Riva, M.; Kubicek, M.; Hao, X.; Franceschi, G.; Gerhold, S.; Schmid, M.; Hutter, H.; Fleig, J.; Franchini, C.; Yildiz, B.; Diebold, U. Influence of Surface Atomic Structure Demonstrated on Oxygen Incorporation Mechanism at a Model Perovskite Oxide. *Nat. Commun.* **2018**, *9*, 3710.
(28) Yoon, J.; Cho, S.; Kim, J.-H.; Lee, J.; Bi, Z.; Serquis, A.; Zhang, X.; Manthiram, A.; Wang, H. Vertically Aligned Nanocomposite Thin Films as a Cathode/electrolyte Interface Layer for Thin-Film Solid Oxide Fuel Cells. *Adv. Funct. Mater.* **2009**, *19*, 3868−3873.
(29) Plonczak, P.; Søgaard, M.; Bieberle-Hütter, A.; Hendriksen, P. V.; Gauckler, L. J. Electrochemical Characterization of La 0.58 Sr 0.4 Co 0.2 Fe 0.8 O 3−δ Thin Film Electrodes Prepared by Pulsed Laser Deposition. *J. Electrochem. Soc.* **2012**, *159*, B471−B482.
(30) Obradors, X.; Puig, T. Coated Conductors for Power Applications: Materials Challenges. *Supercond. Sci. Technol.* **2014**, *27*, 044003.
(31) Usoskin, A.; Betz, U.; Dietrich, R.; Schlenga, K. Long HTS Coated Conductor Processed via Large-Area PLD/ABAD for High-Field Applications. *IEEE Trans. Appl. Supercond.* **2016**, *26*, 1−4.
(32) Buckeridge, J.; Scanlon, D. O.; Walsh, A.; Catlow, C. R. A.; Sokol, A. A. Dynamical Response and Instability in Ceria under Lattice Expansion. *Phys. Rev. B: Condens. Matter Mater. Phys.* **2013**, *87*, 214304.
(33) Niu, G.; Schubert, M. A.; d'Acapito Acapito, F.; Zoellner, M. H.; Schroeder, T.; Boscherini, F. On the Local Electronic and Atomic Structure of Ce1-xPrxO2-δ Epitaxial Films on Si. *J. Appl. Phys.* **2014**, *116*, 123515.
(34) Smith, M.; Choi, Y. S.; Boughey, C.; Kar-Narayan, S. Controlling and Assessing the Quality of Aerosol Jet Printed Features for Large Area and Flexible Electronics. *Flexible Printed Electron.* **2017**, *2*, 015004.
(35) Chen, X.; Wu, N. J.; Smith, L.; Ignatiev, A. Thin-Film Heterostructure Solid Oxide Fuel Cells. *Appl. Phys. Lett.* **2004**, *84*, 2700−2702.
(36) Nishi, Y.; Inoue, N.; Watanabe, K.; Morishita, T.; Shima, T. Ion Milling of Nitrized 18-8 Stainless Steel. *J. Mater. Sci. Lett.* **1987**, *6*, 63−64.
(37) Shimizu, M.; Yamada, T.; Sasaki, K.; Takada, A.; Nomura, H.; Iguchi, F.; Yugami, H. Anisotropic Multi-Step Etching for Large-Area Fabrication of Surface Microstructures on Stainless Steel to Control Thermal Radiation. *Sci. Technol. Adv. Mater.* **2015**, *16*, 025001.
(38) Yu, Y.; Ludwig, K. F.; Woicik, J. C.; Gopalan, S.; Pal, U. B.; Kaspar, T. C.; Basu, S. N. Effect of Sr Content and Strain on Sr Surface Segregation of La1-xSrxCo0.2Fe0.8O3-δ as Cathode Material for Solid Oxide Fuel Cells. *ACS Appl. Mater. Interfaces* **2016**, *8*, 26704−26711.
(39) Smith, C. R.; Sloppy, J. D.; Wu, H.; Santos, T. S.; Karapetrova, E.; Kim, J.-W.; Ryan, P. J.; Taheri, M. L.; May, S. J. Structural Investigation of Perovskite Manganite and Ferrite Films on Yttria-Stabilized Zirconia Substrates. *J. Electrochem. Soc.* **2012**, *159*, F436−F441.
(40) Choi, Y.; Lin, M. C.; Liu, M. Computational Study on the Catalytic Mechanism of Oxygen Reduction on La0.5Sr0.5MnO3 in Solid Oxide Fuel Cells. *Angew. Chem., Int. Ed.* **2007**, *46*, 7214−7219.
(41) Wang, Z.; Peng, R.; Zhang, W.; Wu, X.; Xia, C.; Lu, Y. Oxygen Reduction and Transport on the La1-xSrxCo 1-yFeyO3-δ Cathode in Solid Oxide Fuel Cells: A First-Principles Study. *J. Mater. Chem. A* **2013**, *1*, 12932−12940.
(42) Develos-Bagarinao, K.; De Vero, J.; Kishimoto, H.; Ishiyama, T.; Yamaji, K.; Horita, T.; Yokokawa, H. Oxygen Surface Exchange Properties and Surface Segregation Behavior of Nanostructured La0.6Sr0.4Co0.2Fe0.8O3-δ Thin Film Cathodes. *Phys. Chem. Chem. Phys.* **2019**, *21*, 7183−7195.
(43) Chen, A.; Bi, Z.; Jia, Q.; Macmanus-Driscoll, J. L.; Wang, H. Microstructure, Vertical Strain Control and Tunable Functionalities in Self-Assembled, Vertically Aligned Nanocomposite Thin Films. *Acta Mater.* **2013**, *61*, 2783−2792.
(44) Huang, J.; MacManus-Driscoll, J. L.; Wang, H. New Epitaxy Paradigm in Epitaxial Self-Assembled Oxide Vertically Aligned Nanocomposite Thin Films. *J. Mater. Res.* **2017**, *32*, 4054−4066.
(45) Acosta, M.; Baiutti, F.; Wang, X.; Cavallaro, A.; Wu, J.; Li, W.; Paker, S. C.; Aguadero, A.; Wang, H.; Tarancón, A.; MacManus-Driscoll, J. L. Ultrafast Oxygen Reduction Kinetics in (La,Sr)(Co,Fe)-

https://dx.doi.org/10.1021/acsami.0c15368
ACS Appl. Mater. Interfaces 2021, 13, 4117−4125

O3 Vertically Aligned Nanocomposites below 400 °C. Submitted **2020**.
(46) Macmanus-Driscoll, J. L. Self-Assembled Heteroepitaxial Oxide Nanocomposite Thin Film Structures: Designing Interface-Induced Functionality in Electronic Materials. *Adv. Funct. Mater.* **2010**, *20*, 2035−2045.
(47) Sun, X.; MacManus-Driscoll, J. L.; Wang, H. Spontaneous Ordering of Oxide-Oxide Epitaxial Vertically Aligned Nanocomposite Thin Films. *Annu. Rev. Mater. Res.* **2020**, *50*, 229−253.
(48) MacManus-Driscoll, J. L.; Zerrer, P.; Wang, H.; Yang, H.; Yoon, J.; Fouchet, A.; Yu, R.; Blamire, M. G.; Jia, Q. Strain Control and Spontaneous Phase Ordering in Vertical Nanocomposite Heteroepitaxial Thin Films. *Nat. Mater.* **2008**, *7*, 314−320.
(49) Magnesium Oxide (MgO) Crystal Structure, Lattice Parameters, Thermal Expansion. In *II-VI and I-VII Compounds; Semimagnetic Compounds*; Madelung, O., Rössler, U., Schulz, M.r.; Springer, 2005; pp 1−6.
(50) Singh, S.; Sangle, A. L.; Wu, T.; Khare, N.; MacManus-Driscoll, J. L. Growth of Doped SrTiO3 Ferroelectric Nanoporous Thin Films and Tuning of Photoelectrochemical Properties with Switchable Ferroelectric Polarization. *ACS Appl. Mater. Interfaces* **2019**, *11*, 45683−45691.
(51) Jiang, J.; Hertz, J. L. On the Variability of Reported Ionic Conductivity in Nanoscale YSZ Thin Films. *J. Electroceram.* **2014**, *32*, 37−46.
(52) Rupp, G. M.; Opitz, A. K.; Nenning, A.; Limbeck, A.; Fleig, J. Real-Time Impedance Monitoring of Oxygen Reduction during Surface Modification of Thin Film Cathodes. *Nat. Mater.* **2017**, *16*, 640−645.
(53) Çelikbilek, Ö.; Jauffrès, D.; Siebert, E.; Dessemond, L.; Burriel, M.; Martin, C. L.; Djurado, E. Rational Design of Hierarchically Nanostructured Electrodes for Solid Oxide Fuel Cells. *J. Power Sources* **2016**, *333*, 72−82.
(54) Shen, F.; Lu, K. Comparison of Different Perovskite Cathodes in Solid Oxide Fuel Cells. *Fuel Cells* **2018**, *18*, 457−465.
(55) Sempolinski, D. R.; Kingery, W. D. Ionic Conductivity and Magnesium Vacancy Mobility in Magnesium Oxide. *J. Am. Ceram. Soc.* **1980**, *63*, 664−669.
(56) Chevalier, S.; Caboche, G.; Przybylski, K.; Brylewski, T. Effect of Nano-Layered Ceramic Coatings on the Electrical Conductivity of Oxide Scale Grown on Ferritic Steels. *J. Appl. Electrochem.* **2009**, *39*, 529−534.
(57) Hess, F.; Yildiz, B. Polar or Not Polar? The Interplay between Reconstruction, Sr Enrichment, and Reduction at the La0.75Sr0.25MnO3 (001) Surface. *Phys. Rev. Mater.* **2020**, *4*, 015801.
(58) Jung, W.; Tuller, H. L. Investigation of Surface Sr Segregation in Model Thin Film Solid Oxide Fuel Cell Perovskite Electrodes. *Energy Environ. Sci.* **2012**, *5*, 5370−5378.
(59) Im, H.-N.; Choi, M.-B.; Singh, B.; Lim, D.-K.; Song, S.-J. Investigation of Oxygen Reduction Reaction on La 0.1 Sr 0.9 Co 0.8 Fe 0.2 O 3-δ Electrode by Electrochemical Impedance Spectroscopy. *J. Electrochem. Soc.* **2015**, *162*, F728−F735.
(60) Lu, Y.; Kreller, C.; Adler, S. B. Measurement and Modeling of the Impedance Characteristics of Porous $La_{1-x}Sr_xCoO_3-\delta$ Electrodes. *J. Electrochem. Soc.* **2009**, *156*, B513−B525.

https://dx.doi.org/10.1021/acsami.0c15368
ACS Appl. Mater. Interfaces 2021, 13, 4117−4125